Micromechanical modeling of the machining behavior of natural fiber-reinforced polymer composites

Faissal Chegdani, Mohamed El Mansori, Satish T. S. Bukkapatnam, J. N. Reddy

Micromechanical modeling of the machining behavior of natural fiber-reinforced polymer composites

Faissal Chegdani[1] · Mohamed El Mansori[1,2] · Satish T. S. Bukkapatnam[2] · J. N. Reddy[3]

Abstract
This paper aims to develop a 2D finite element (FE) model at microscale for numerical simulation of the machining behavior of natural fiber-reinforced polymer (NFRP) composites. The main objective of this study is to reproduce the experimentally observed specific cutting behavior of natural fibers within the composite material. Flax fiber-reinforced polypropylene (PP) composites are modeled separately using an elasto-plastic behavior with a ductile damage criterion for flax fibers and PP matrix, while the microscopic interfaces are represented using the cohesive zone modeling (CZM). Numerical outputs are compared with experimental results for the FE model validation. Results show that the proposed FE model can reproduce the cutting force with a good precision for a large cutting speed range (12–80 m/min). The FE model shows also an efficiency and accuracy in predicting the cutting behavior of flax fibers by reproducing the fiber deformation, the fibers torn-off, and the fracture of the interfaces during machining. Moreover, the FE model can be an effective tool for analyzing the quality of the microscopic interfaces in the NFRP composites after machining.

Keywords Natural fiber composites · Machining · Finite element analysis · Experimental correlation

1 Introduction

The use of natural fibers in composite industry has increased in the last decades, thanks to many advantages that these eco-friendly materials can provide for bio-economy. In fact, some natural fibers, especially plant fibers such as flax, jute, or hemp fibers, can be a good substitute to glass fibers commonly used in composite industry. Regarding the growth and processing conditions, some varieties of plant fibers may have better rigidity than glass fibers [1–4]. Moreover, plant fibers offer many other advantages such as vibration damping [5, 6] and acoustic and thermal insulation [7], in addition to both their biodegradability and recyclability that make them advantageous for circular economy and sustainable development [8].

Manufacturing processes of natural fiber-reinforced polymer (NFRP) composites present some technical issues that need scientific investigations, especially for surface finishing by machining processes in order to complete the assembly of the components or industrial parts [9]. Indeed, the multiscale complex cellulosic structure of natural fibers prevents an efficient fiber shearing due to their high transverse elasticity which makes them highly sensitive to the variation of machining process parameters [10–13]. Furthermore, the multiscale random arrangement of the natural fibrous structure that includes the elementary fiber, the technical fiber, the fiber bundle, and the fibers yarn imposes the selection of the pertinent scale for analyzing the machined surfaces of NFRP composites [14]. The multiscale behavior is also present inside each elementary plant fiber. In fact, each elementary fiber is itself a composite material at the microscopic scale with a combination of cellulose microfibrils embedded in amorphous natural polymers (hemicellulose and lignin) [15]. The cellulose microfibrils content and their orientation along the fiber axis, the fiber shape, the fiber diameter, the moisture content, and the lumen size determine the mechanical properties of the elementary fibers [2]. The natural character of all these parameters

✉ Faissal Chegdani
faissal.chegdani@ensam.eu

[1] MSMP Laboratory / EA7350, Arts et Métiers ParisTech, Rue Saint Dominique BP508, 51006 Châlons-en-Champagne, France

[2] Department of Industrial and Systems Engineering, Texas A&M University, 3131 TAMU, College Station, TX 77843, USA

[3] Department of Mechanical Engineering, Texas A&M University, 3123 TAMU, College Station, TX 77843, USA

induces a high variability of the mechanical properties of the natural fibers [2].

Because of the high variability of natural fibers properties, the machinability qualification of NFRP composites with experimental designs is a hard task since the fiber type in this case is not a pertinent parameter for the qualification. For NFRP composites, each new fiber harvest and each new fiber variety must be experimentally tested and validated for the machinability behavior which may be expensive and laborious to achieve. Therefore, developing a numerical modeling for NFRP machining becomes important and essential for industrials to improve the NFRP production in terms of cost and time.

Finite element analysis (FEA) has been extensively used to simulate the machining operations [16–18]. Machining simulations of metallic materials are generally performed with the Johnson–Cook model [19] in order to consider not only the dynamic rate-dependent hardening of the work-material but also the induced thermal effect [20, 21]. In the last several decades, a particular interest was focused on the FEA of the machining operations of synthetic fiber-reinforced polymer (SFRP) composites [22]. Multiscale models have been performed to investigate the effect of heterogeneity structure of the SFRP composites during machining. Indeed, micromechanical models have been developed to explore the cutting behavior of synthetic fibers (such as glass or carbon) and polymer matrix in addition to the interfaces [23–26]. Synthetic fibers have been modeled with an elastic behavior and brittle failure based on the maximum failure stress criterion. Polymer matrices have been modeled with an elasto-plastic behavior and a ductile damage. Interfaces have been usually modeled with the cohesive zone model (CZM) while some researchers consider the interfaces as solid continuum elements [26]. Then, macroscopic models for machining SFRP composites have been performed using Tsai-Hill, Maximum stress, Hashin, or Hoffman criteria [27–32]. All these models consider a brittle fracture of the composite at failure to produce the removed chip. Tsai-Hill and maximum stress criteria seem to behave similarly in terms of predicted cutting forces [28]. However, a comparative study between maximum stresses, Hashin, and Hoffman criteria shows that cutting forces predicted using the Hashin failure criterion are closer to experimental results [31].

For NFRP composites, natural fibers cannot be modeled using the maximum failure stress criterion at microscale. This is because natural fibers have a cellulosic structure that induces a visco-elasto-plastic behavior with both tensile tests [33, 34] and nanoindentation loads [35–37]. Also, Tsai-Hill, maximum stress, Hashin, or Hoffman models cannot be used for machining NFRP composites at macroscale because they consider a brittle failure while the NFRP composites generated a ductile failure in tensile and shear solicitations [38] with a visco-elasto-plastic behavior [39]. Numerical modeling of NFRP composites has been investigated in a few earlier works to reproduce the mechanical behavior of natural fibers at microscale and the NFRP composite at macroscale [40, 41]. However, the numerical modeling of the cutting behavior of natural fibers is not yet investigated and consequently, no finite element analysis results exists for machining NFRP composites at this time.

In this paper, a micromechanical model for NFRP composites is proposed to simulate the cutting behavior of natural fibers, polymer matrix, and the cohesive interfaces. Flax fibers and polypropylene (PP) matrix are considered in this study. A literature review on the mechanical behavior of flax fibers and PP matrix is first performed to determine the mechanical model suitable for each composite component. Then, the micromechanical model is described with the detail of the FEM parameters. The numerical results are next discussed and compared with the experimental results in order to validate the finite element model.

2 FEM for micromechanical machining of NFRP composites

2.1 Flax fiber modeling

In general, natural fibers have a cellulosic structure with a stacking of cell walls with an internal cavity called “lumen” as shown in Fig. 1. Each cell wall is itself a composite material of cellulose microfibrils embedded in natural amorphous polymers of hemicellulose and lignin [15]. The major cell wall that controls the fiber behavior is “S2” with its high cross section. In the cell wall S2, the cellulose microfibrils are oriented with a small angle called the microfibrils angle “θ” [15]. This cellulosic structure of natural fibers induces an orthotropic behavior and the mechanical behavior of the elementary flax fiber depends on the cellulose microfibrils orientation toward the fiber axis.

Tensile tests on elementary flax fibers show a non-linearity in the mechanical behavior. Indeed, Fig. 2(b) allows discriminating three mechanical behavior zones for flax fibers [15, 33]:

- Zone I: linear elastic behavior that corresponds to first mechanical response of the initial cellulose microfibrils structure
- Zone II: non-linear plastic behavior that corresponds to rearrangement of cellulose microfibrils by the tensile motion to be as parallel as possible to the fiber axis
- Zone III: linear elastic behavior that corresponds to the second mechanical response of the cellulose microfibrils structure after rearrangement

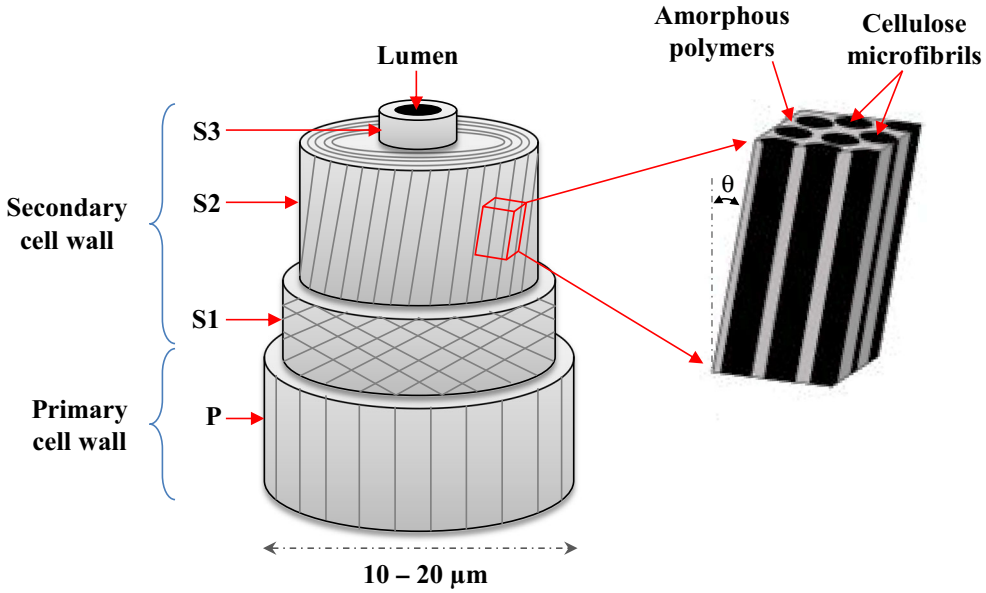

Fig. 1 Schematic depiction of the microscopic structure of an elementary flax fiber showing the cellulosic structure inside the secondary cell wall S2 (figure redrawn from [42])

The alignment of cellulose microfibrils induces rearrangements in the core of the surrounding amorphous matrix and, therefore, the cellulosic reorganization implies an elasto-visco-plastic deformation [33]. Consequently, natural fibers cannot be modeled as synthetic fibers (glass and carbon) using an elastic behavior. In the case of flax fibers, a plastic behavior should be considered before fiber failure for the FEM study.

The elastic behavior of flax fiber is modeled using the anisotropic properties given in Table 1. As well known in the literature, the mechanical properties of natural fibers present a high variability due to many factors such as the climatic conditions of growth (chemical composition) and the mechanical conditions of extraction in addition to the chemical treatment for enhancing the interfacial strength. For example, flax fibers have a tensile modulus between 27 and 103 GPa, a tensile strength between 343 and 2000 MPa, and an elongation between 1.2 and 3.3% [2]. Flax fiber shear strength has been found between 10 and 50 MPa [40]. Therefore, the mechanical parameters in Table 1 are chosen to be as close as possible to those of flax fibers used in the experimental part. The considered values in Table 1 are closer to the flax stiffness and strength values used in [40].

The longitudinal plastic behavior (in the tensile direction) is implemented using 29 points on the yield stress versus plastic strain curve from Fig. 2 with a maximum yield stress of 750 MPa. The Hill's potential function is used to implement the anisotropic plasticity-based failure for flax fibers. Hill's potential function is a simple extension of the Mises function, which can be expressed in terms of rectangular Cartesian stress components (σ_{ij}) as following [40, 45]:

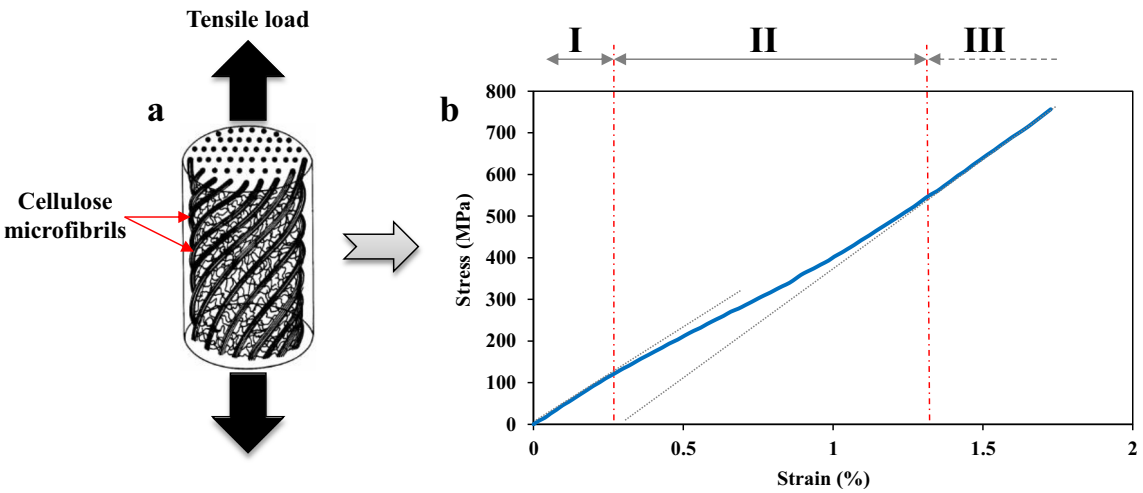

Fig. 2 (a) Principle of flax fiber structure showing the helical arrangement of cellulose microfibrils (adapted from [43]). (b) Typical stress–strain curve for flax fiber (adapted from [44])

Table 1 Mechanical properties of flax fiber used in the FEM

Property	Direction	Value	Unit
Elastic modulus	E_{11}	50	GPa
	$E_{22} = E_{33}$	12	
	$G_{12} = G_{13} = G_{23}$	3.4	
Poisson's ratio	ν_{12}	0.178	–
	$\nu_{13} = \nu_{23}$	0.2	
Strength	S_{11}	750	MPa
	$S_{22} = S_{33}$	150	
	$S_{12} = S_{13} = S_{23}$	20	

Table 2 Mechanical properties of PP matrix used in the FEM

Property	Value	Unit
Elastic modulus	2.1	GPa
Poisson's ratio	0.4	–
Yield strength	35	MPa
Failure strength	30	MPa

$$f(\sigma) = \sqrt{F(\sigma_{22}-\sigma_{33})^2 + G(\sigma_{33}-\sigma_{11})^2 + H(\sigma_{11}-\sigma_{22})^2 + 2L\sigma_{23}^2 + 2M\sigma_{31}^2 + 2M\sigma_{12}^2} \tag{1}$$

where F, G, H, L, M, and N are constants defined as the following:

$$F = \frac{(\sigma^0)^2}{2}\left(\frac{1}{\overline{\sigma}_{22}^{\,2}} + \frac{1}{\overline{\sigma}_{33}^{\,2}} - \frac{1}{\overline{\sigma}_{11}^{\,2}}\right) = \frac{1}{2}\left(\frac{1}{R_{22}^2} + \frac{1}{R_{33}^2} - \frac{1}{R_{11}^2}\right) \tag{2}$$

$$G = \frac{(\sigma^0)^2}{2}\left(\frac{1}{\overline{\sigma}_{33}^{\,2}} + \frac{1}{\overline{\sigma}_{11}^{\,2}} - \frac{1}{\overline{\sigma}_{22}^{\,2}}\right) = \frac{1}{2}\left(\frac{1}{R_{33}^2} + \frac{1}{R_{11}^2} - \frac{1}{R_{22}^2}\right) \tag{3}$$

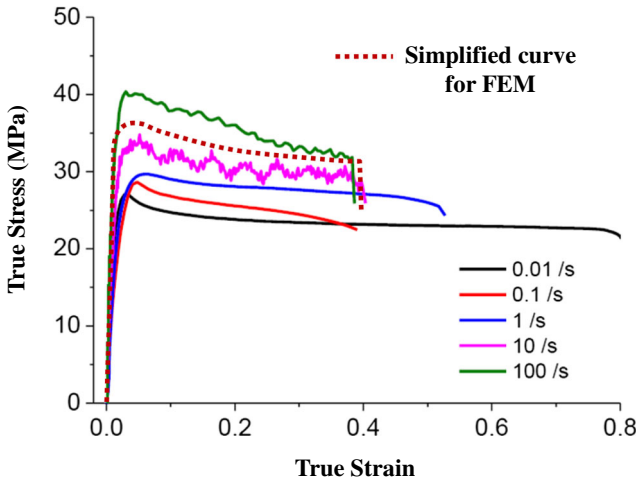

Fig. 3 Stress–strain curves of polypropylene at different strain rate showing the simplified curve used for the numerical modeling (adapted from [48])

$$H = \frac{(\sigma^0)^2}{2}\left(\frac{1}{\overline{\sigma}_{11}^{\,2}} + \frac{1}{\overline{\sigma}_{22}^{\,2}} - \frac{1}{\overline{\sigma}_{33}^{\,2}}\right) = \frac{1}{2}\left(\frac{1}{R_{11}^2} + \frac{1}{R_{22}^2} - \frac{1}{R_{33}^2}\right) \tag{4}$$

$$L = \frac{3}{2}\left(\frac{\tau^0}{\overline{\sigma}_{23}}\right)^2 = \frac{3}{2R_{23}^2} \tag{5}$$

$$M = \frac{3}{2}\left(\frac{\tau^0}{\overline{\sigma}_{13}}\right)^2 = \frac{3}{2R_{13}^2} \tag{6}$$

$$N = \frac{3}{2}\left(\frac{\tau^0}{\overline{\sigma}_{12}}\right)^2 = \frac{3}{2R_{12}^2} \tag{7}$$

where each $\overline{\sigma}_{ij}$ is the measured yield stress value when σ_{ij} is applied as the only nonzero stress component, $\tau^0 = \frac{\sigma_0}{\sqrt{3}}$, where σ_0 is the reference yield stress which is set to be equal to σ_{11} in this case; R_{ij} are anisotropic yield stress ratios that are needed to implement the Hill's potential function in the FEM [45] and are defined as follows where the considered strength values are provided in Table 1:

$$R_{11} = \frac{\overline{\sigma}_{11}}{\sigma^0} \tag{8}$$

$$R_{22} = \frac{\overline{\sigma}_{22}}{\sigma^0} \tag{9}$$

$$R_{33} = \frac{\overline{\sigma}_{33}}{\sigma^0} \tag{10}$$

$$R_{12} = \frac{\overline{\sigma}_{12}}{\tau^0} \tag{11}$$

Table 3 Mechanical properties of CZM used in the FEM [40]

Property	Direction	Value	Unit
Stiffness	$K_{nn} = K_{ss} = K_{tt}$	27.96	GPa mm^{-1}
	$K_{ns} = K_{nt} = K_{st}$	0	
Failure strength	$t_n^0 = t_s^0 = t_t^0$	28.5	MPa
Failure energy	$G_n = G_s = G_t$	4	J/m^2

$$R_{13} = \frac{\overline{\sigma}_{13}}{\tau^0} \tag{12}$$

$$R_{23} = \frac{\overline{\sigma}_{23}}{\tau^0} \tag{13}$$

Unlike synthetic fibers, natural fibers induce an elasto-plastic behavior with ductile failure. Therefore, a ductile criterion [46] is considered to model the flax fiber failure. The ductile criterion is based on a fracture diagram which gives the equivalent plastic strain at fracture as a function of the stress state. The model assumes that the equivalent plastic strain at the onset of damage is a function of stress triaxiality and strain rate. The criterion for damage initiation is met when the following condition is satisfied [46]:

$$\int_0^{\bar{\varepsilon}_{eq}^{**}} \frac{d\varepsilon_{eq}}{\varepsilon_{eq}^{**}\left(\eta, \dot{\varepsilon}^{pl}\right)} = 1 \tag{14}$$

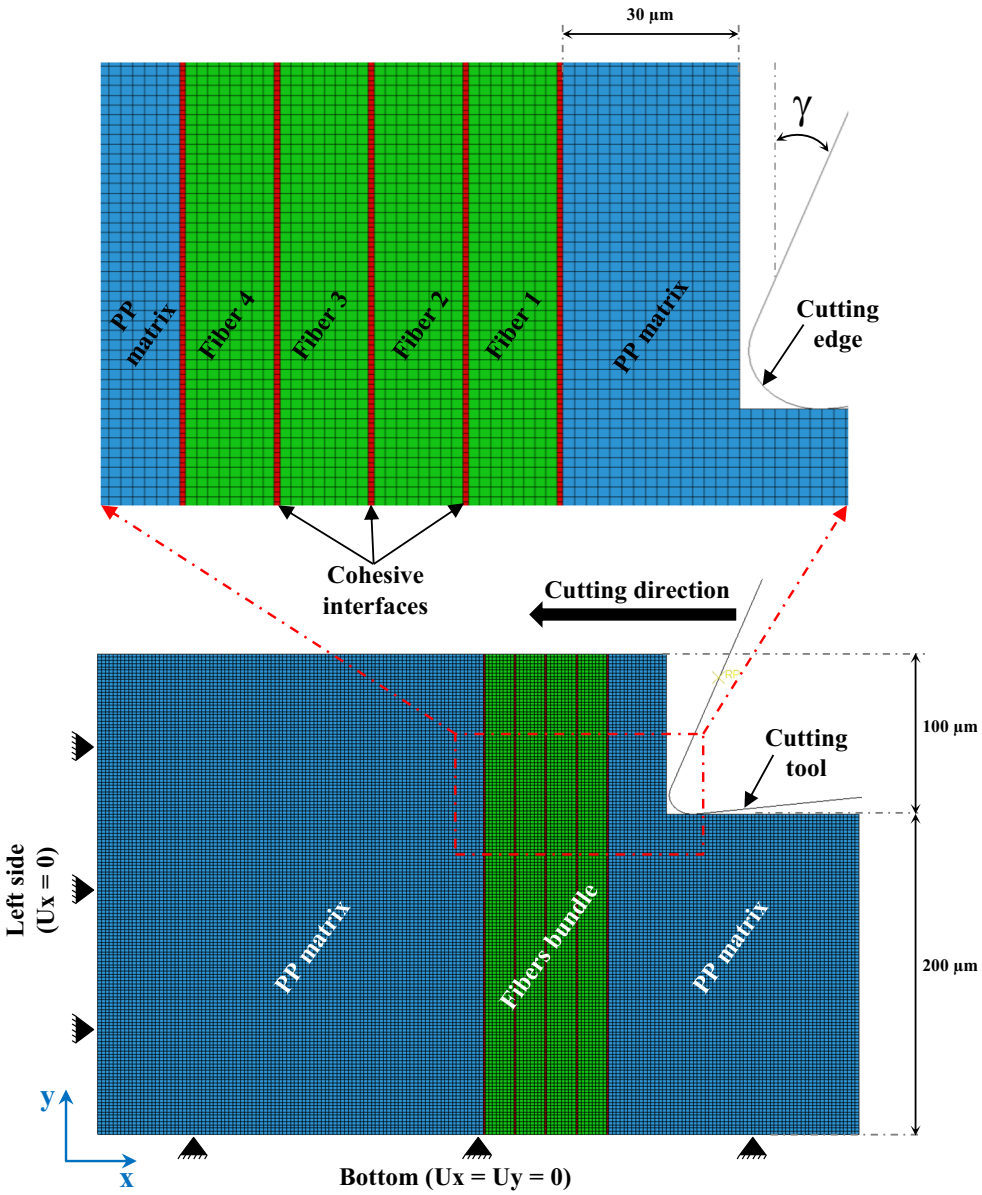

Fig. 4 Overview image of the micromechanical cutting model for NFRP composites with a zoom on the active zone showing the three phases, the tool geometry, and the boundary conditions

where ε_{eq} is the equivalent plastic strain, ε_{eq}^{**} is the equivalent plastic strain at fracture, $\dot{\varepsilon}^{pl}$ is the equivalent plastic strain rate, and η is stress triaxiality that can be calculated by the following equations [47]:

$$\eta = \frac{\sigma_m}{\sigma_{eq}} \tag{15}$$

Here σ_m denotes the hydrostatic stress and σ_{eq} is the Von Mises equivalent stress that can be calculated by the following equations:

$$\sigma_m = \frac{\sigma_{11} + \sigma_{22} + \sigma_{33}}{3} \tag{16}$$

$$\sigma_{eq} = \sqrt{\frac{1}{2}\left[(\sigma_{11}-\sigma_{22})^2 + (\sigma_{22}-\sigma_{33})^2 + (\sigma_{33}-\sigma_{11})^2 + 6\left(\sigma_{12}^2 + \sigma_{23}^2 + \sigma_{31}^2\right)\right]} \tag{17}$$

As for the Hill's potential function, the stress triaxiality criterion is calculated using the strength values of Table 1.

2.2 Polypropylene matrix modeling

Polypropylene matrix is also modeled using an elasto-plastic behavior with a ductile damage. However, mechanical properties of thermoplastic polymers are strongly dependent of the strain rate. Therefore, for modeling a machining operation, it is more efficient to implement the dynamic mechanical properties of PP matrix obtained at high strain rates. Figure 3 shows the stress-strain curves of PP polymer at different strain rate values from quasi-static mode to dynamic mode [48]. It can be seen that increasing the strain rate increases slightly the elastic slope, increases the yield stress, and reduces significantly the strain at failure. A simplified curve as shown in Fig. 3 is considered to implement the isotropic plastic behavior of PP matrix using 36 points on the yield stress versus plastic strain curve with a maximum yield stress of 35 MPa. From the high strain rate curves of Fig. 3, the elastic modulus of PP is found to be equal to 2.1 GPa.

Due to the ductile behavior of PP, the ductile criterion described in Section 2.1 is also suitable for modeling the ductile failure of the matrix. The stress triaxiality of PP at high strain rate is given in [48] and it is found to be equal to 0.33 at a strain rate of 10 s^{-1}. Table 2 summarizes the mechanical parameter of PP matrix used for modeling.

2.3 Interfaces modeling

Interfaces are modeled using the cohesive zone model (CZM). The elastic behavior of the CZM is modeled using a linear elastic traction-separation behavior. It assumes initially linear elastic behavior followed by the initiation and evolution of damage. The elastic behavior is written in terms of an elastic constitutive matrix that relates the nominal stresses to the nominal strains across the interface following the equation [45]:

$$\begin{Bmatrix} t_n \\ t_s \\ t_t \end{Bmatrix} = \begin{bmatrix} K_{nn} & K_{ns} & K_{nt} \\ K_{ns} & K_{ss} & K_{st} \\ K_{nt} & K_{st} & K_{tt} \end{bmatrix} \begin{Bmatrix} \varepsilon_n \\ \varepsilon_s \\ \varepsilon_t \end{Bmatrix} \tag{18}$$

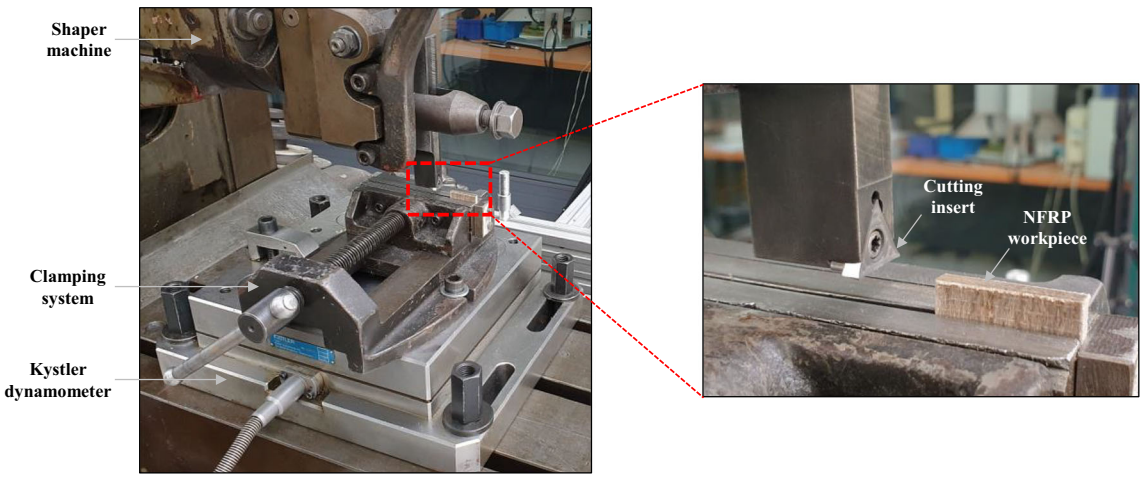

Fig. 5 Experimental setup used for orthogonal cutting tests of NFRP composites

Table 4 Cutting conditions used for FEM and experimental tests

	Parameter	Value	Unit
Tool geometry	Rake angle (γ)	20	Degree (°)
	Clearance angle (α)	7	Degree (°)
	Edge radius (r_ε)	12	µm
Cutting parameters	Depth of cut (a_p)	100	µm
	Cutting speed (V_c)	12/20/32/50/80	m/min

where t_n, t_s, and t_t are the nominal stresses in the normal, shear, and tangential directions, respectively. K_{ij} are the components of the elasticity matrix. ε_n, ε_s, and ε_t are the nominal strains in the normal, shear, and tangential directions, respectively. The corresponding separations are denoted by δ_n, δ_s, and δ_t and are defined as the following, where T_0 is the initial thickness of the cohesive element [45]:

$$\varepsilon_n = \frac{\delta_n}{T_0}, \varepsilon_s = \frac{\delta_n}{T_0}, \varepsilon_t = \frac{\delta_t}{T_0} \tag{19}$$

Damage is assumed to initiate when a quadratic interaction function involving the nominal stress ratios reaches a value of one. This criterion can be represented as the following [40, 45]:

$$\left(\frac{\langle t_n \rangle}{t_n^0}\right)^2 + \left(\frac{t_s}{t_s^0}\right)^2 + \left(\frac{t_t}{t_t^0}\right)^2 = 1 \tag{20}$$

t_n^0, t_s^0, and t_t^0 are the peak values of the nominal stress components in the normal, shear, and tangential directions, respectively. The symbol $\langle\rangle$ represents the Macaulay bracket which is used to signify that a pure compressive deformation or stress state does not initiate damage [45]. Table 3 gives the considered mechanical parameters of the cohesive element that was collected from [40] where strength parameters are obtained by micro-bond experiments and stiffness parameters are calculated using micro-bond simulations.

2.4 FEM setup

FEM study is performed with Abaqus/Explicit software (version 6.11-2) [45]. A 2D micromechanical model is considered for simulation the orthogonal cutting of flax fiber-reinforced PP matrix. Therefore, flax fibers, PP matrix, and cohesive interfaces are considered as a separate phase. As shown in Fig. 4, a bundle of four elementary fibers is modeled inside

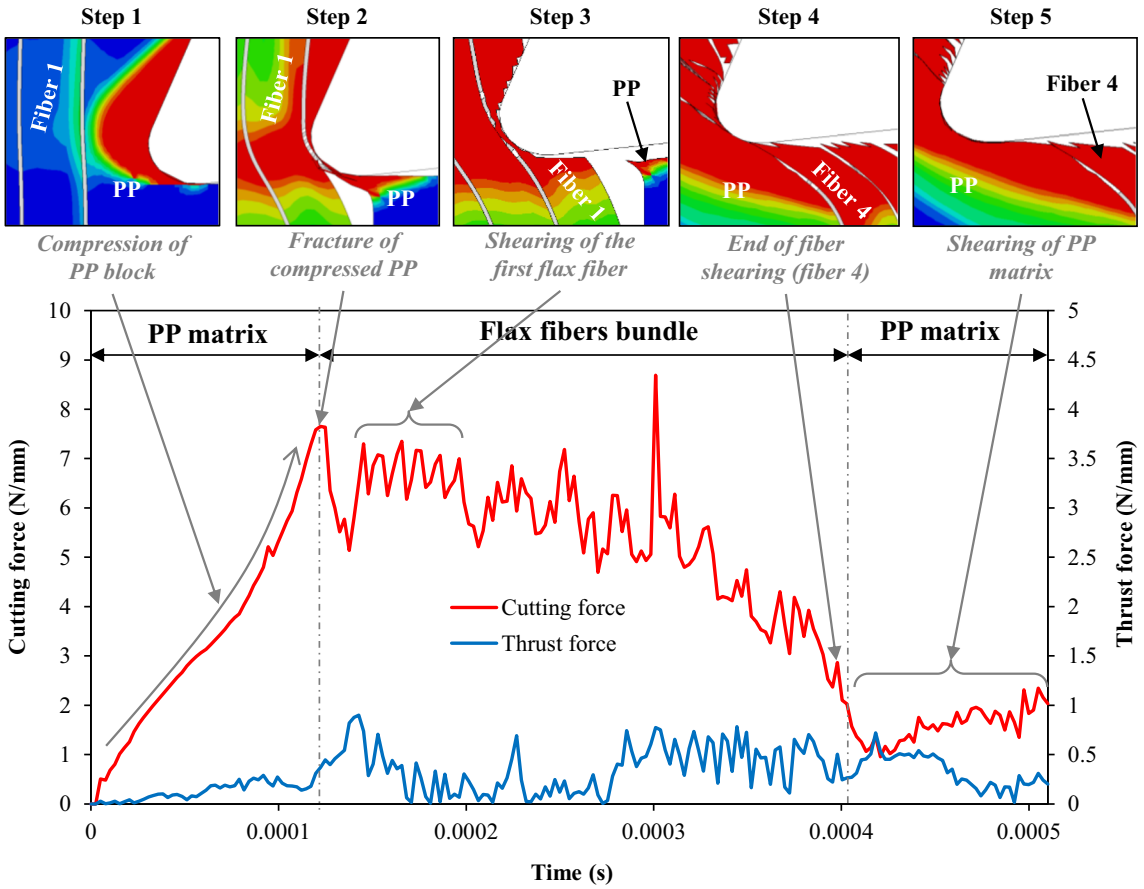

Fig. 6 Evolution of the machining forces regarding the tool/NFRP interactions for V_c = 20 m/min

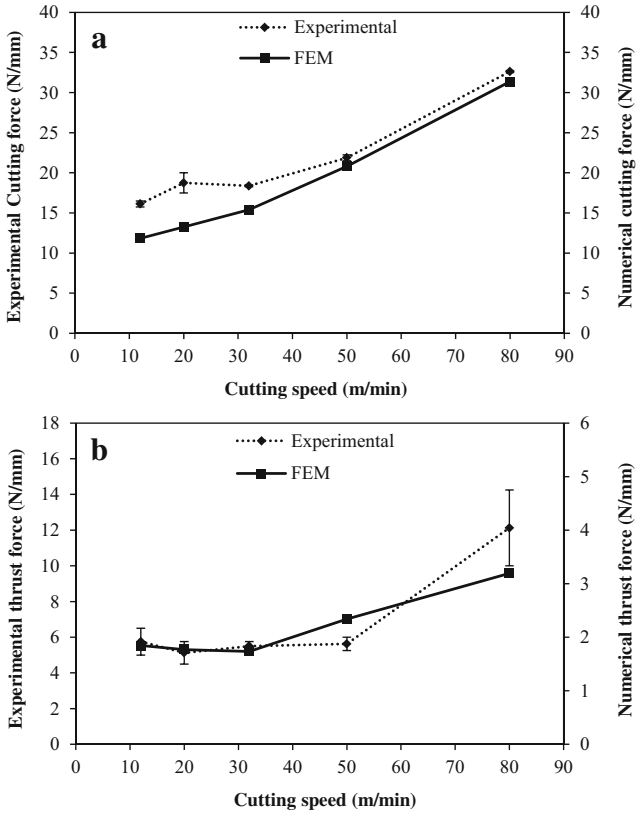

Fig. 7 Comparison between FEM and experimental machining forces. (a) Cutting forces. (b) Thrust forces

the PP matrix. Flax fibers are oriented perpendicularly to the cutting direction. Each elementary fiber has a diameter of 15 μm. CZM elements with 1 μm of thickness are inserted to model the fiber/matrix interfaces and the fiber/fiber interfaces. A plane stress analysis, which is more suitable for FEM cutting of composites [31], is considered in this study. The cutting tool is considered as an analytical rigid body and a reference point controls the movement of the cutting tool. Both flax fibers and PP matrix are meshed with 4-node bilinear plane stress quadrilateral elements (CPS4R) and 2 μm of mesh size. Cohesive interfaces are meshed with a 4-node two-dimensional cohesive element (COH2D4) and 1 μm of mesh size. The frictional contacts between the cutting tool and the two phases (fiber and matrix) were assumed in the model to be controlled by the Coulomb friction law. A previous author's work with nano-scratching shows that the dynamic friction coefficient is around 0.5 for flax fibers and 0.4 for PP matrix at the highest values of scratching speed and scratching load that were considered [37]. These values of the friction coefficient are used for the FEM study for the contact between the tool and each NFRP phase.

The current micromechanical cutting model contains a very small elements (1–2 μm), which forces Abaqus/Explicit to use a small time increment to integrate the entire model in time. By scaling the masses of these controlling elements at the beginning of the step (applying a mass scaling factor), the stable time increment can be increased significantly [45]. Indeed, during the cutting analysis, elements near the cutting zone typically experience large amounts of deformation. The reduced characteristic lengths of these elements result in a smaller global time increment. Scaling the mass of these elements throughout the simulation can significantly decrease the computation time and limits the violation of elements aspect ratios. For cases in which the compressed elements are impacting a stationary rigid body (i.e., the cutting tool), increases in mass for these small elements during the simulation will have very little effect on the overall dynamic response [45]. For the current FEM study, many mass scaling factor (MSF) values have been tested with the mesh size of 1–2 μm and it has been found that a MSF of 40,000 is efficient for the micromechanical cutting model of NFRP. For comparison, the mass scaling technique has been previously used to enhance the computational efficiency of a metallic end milling model with a MSF = 7404 for a mesh size of 6.6–10 μm [49].

2.5 Experimental validation

Orthogonal cutting experiments are performed on a shaper machine (GSP-EL 136) for unidirectional flax fiber-reinforced PP composite workpieces (see Fig. 5). As for the FE model, flax fibers are oriented perpendicularly to the cutting direction. A carbide cutting tool (TCGX 16 T3 04-AL A7CA) provided by "Sandvik Coromant – FR" is fixed to the moving saddle. Then, the edge trimming of the composite material results from the relative motion between the tool and the clamped workpiece. Each NFRP workpiece has the dimensions of 30 × 15 × 4 mm. A piezoelectric dynamometer is inserted under the workpiece clamping system to capture the cutting forces. The machined surfaces are analyzed using a scanning electron microscope (JSM-5510LV) at low vacuum mode in order to compare the real cutting behavior of flax fibers with the FEM outputs. Table 4 presents the cutting conditions considered for both the FEM and the experimental tests.

3 Results and discussion

3.1 Micromechanical FEM cutting process of NFRP composites

Figure 6 shows the typical evolution of the machining forces at each cutting stage through the micro-geometrical model. The cutting starts by the contact interaction of the cutting edge with the first PP block (step 1 in Fig. 6). The high plasticity of the PP matrix induces a high plastic compression of the first PP block which increases progressively the reaction force until reaching the fracture of the compressed PP block and, then, relaxation of the reaction force. The compression of the first

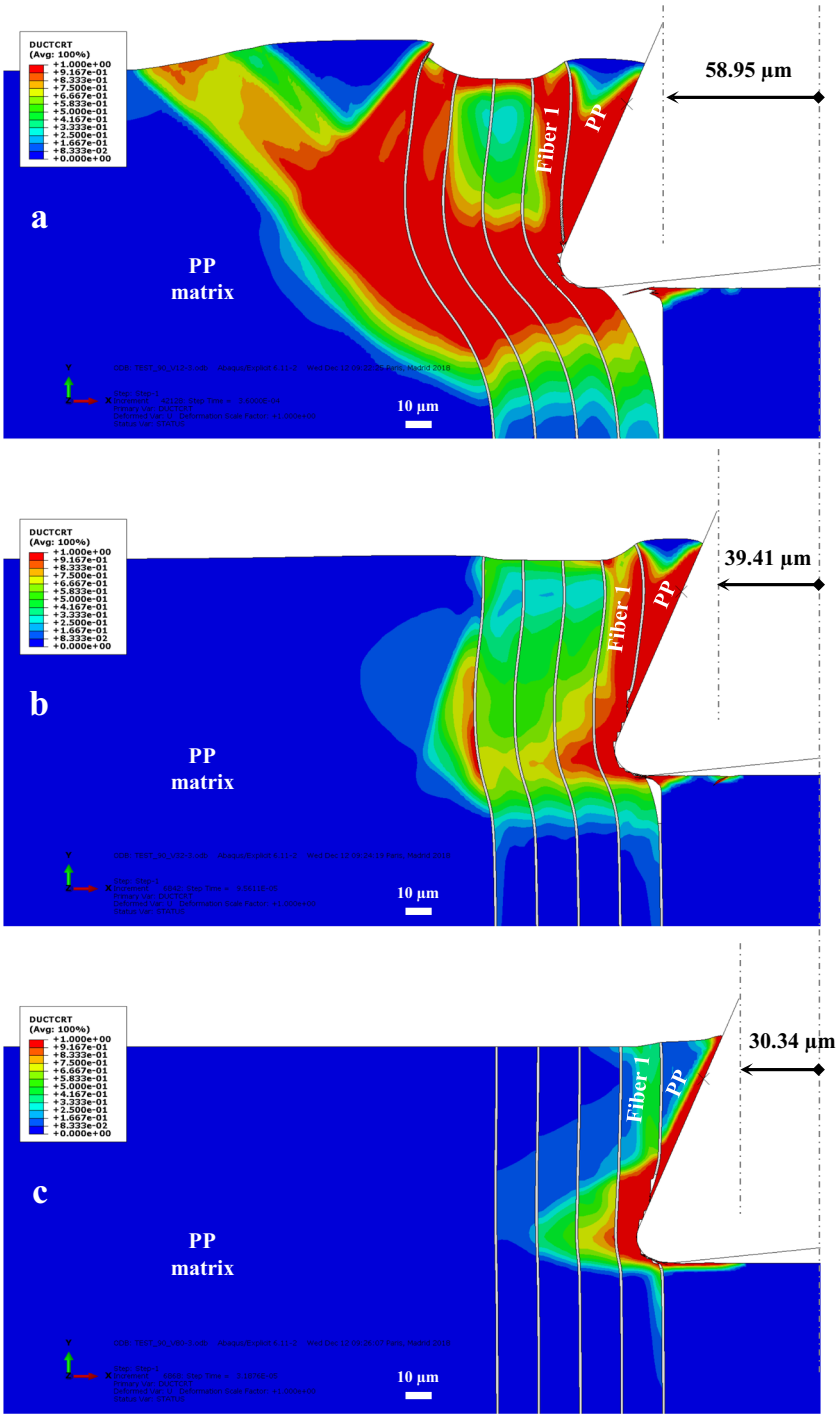

Fig. 8 FEM ductile criterion map at the beginning of the first fiber shearing in the NFRP model. (a) $V_c = 12$ m/min. (b) $V_c = 32$ m/min. (c) $V_c = 80$ m/min

PP block is accompanied with a transverse deformation of the first flax fiber (step 2 in Fig. 6). After the PP fracture, the first deformed fiber starts shearing (step 3 in Fig. 6) followed by the other elementary fibers in the bundle. The cutting force decreases when shearing the last fibers because these fibers are highly deformed and damaged (step 4 in Fig. 6). Finally, the cutting tool is engaged in the second PP matrix block (step 5 in Fig. 6). The thrust force is significantly lower than the cutting force and reaches its maximum at two cutting stages: at the first tool engagement with the first fiber engagement and when shearing the last fibers in the bundles that are highly deformed. This can be explained by the normal spring-back force applied by the fiber when it is transversally deformed.

3.2 FEM prediction of the machining forces

In the proposed 2D micromechanical model, machining forces are acquired on PP matrix and flax fibers separately. This is

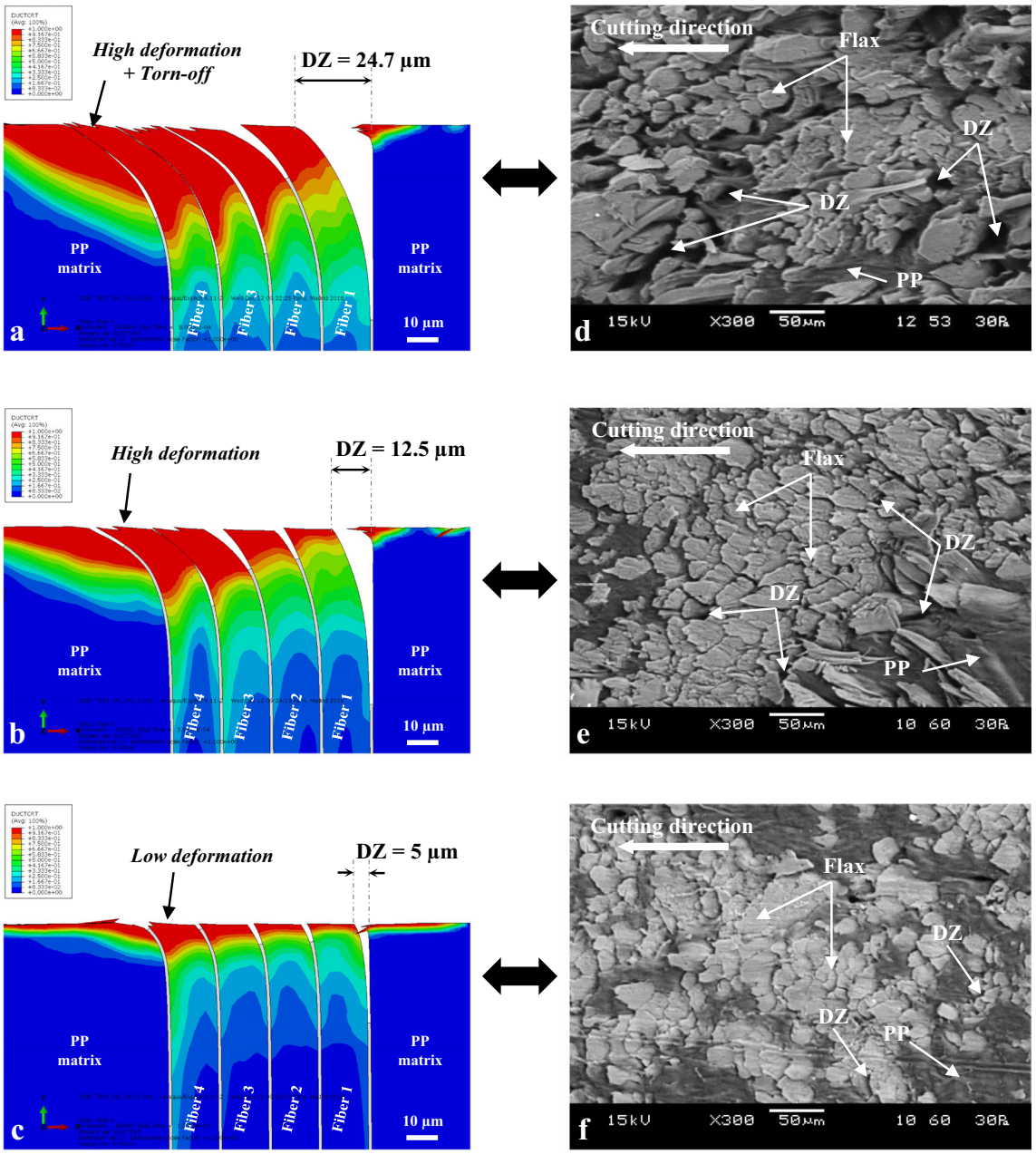

Fig. 9 Comparison of fiber cutting behavior between FEM and experiments. FEM results are for (a) V_c = 12 m/min, (b) V_c = 32 m/min, and (c) V_c = 80 m/min. Experimental results are the SEM images of machined surfaces for (d) V_c = 12 m/min, (e) V_c = 32 m/min, and (f) V_c = 80 m/min. "DZ" means the deboning zone

not the case for the cutting forces acquired from experimental tests where measured forces concern the cutting of all the composite phases at the same time. Therefore, the cutting force is calculated as the sum of reaction force when the fracture of the compressed PP (step 2 in Fig. 6) and the mean reaction force through the flax fiber bundle. The thrust force is calculated as the sum of the mean reaction force through the PP and the mean reaction force through the flax bundles. To have comparable results between FEM and experiments, the ratio between the machining force the sample width is considered for the analysis.

To validate the FE model in terms of machining forces, Fig. 7 shows a comparison between FEM and experimental machining forces. Globally, FEM results provide the same experimental trend in terms of both cutting and thrust forces. Indeed, no significant difference is noticed from V_c = 12 m/min to V_c = 32 m/min. Then, both cutting and thrust force increase significantly by cutting speed increase until V_c = 80/ min. When comparing the magnitudes, FEM cutting forces have similar magnitudes as the experimental results (Fig. 7(a)). However, FEM thrust forces are significantly lower than experimental thrust forces. Indeed, as shown in

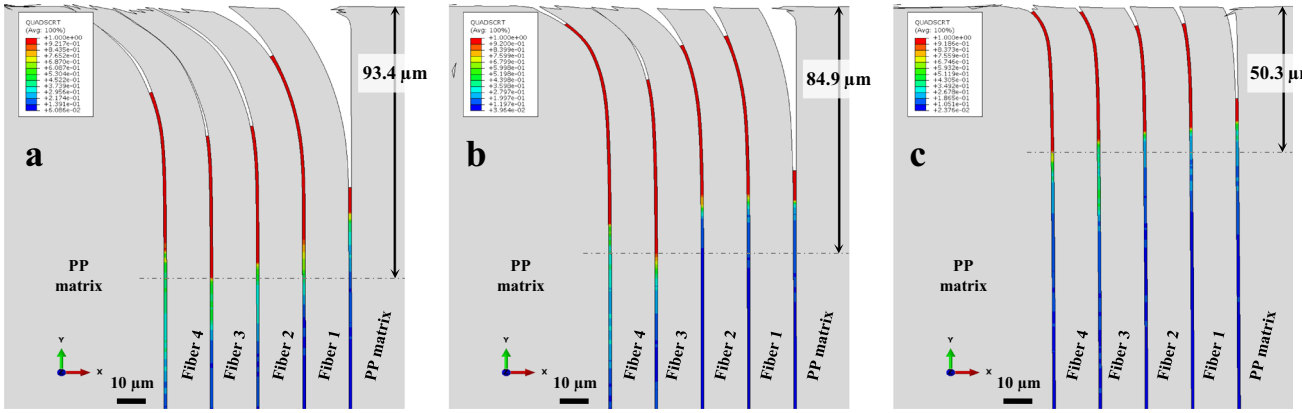

Fig. 10 FEM quadratic criterion map on the cohesive interfaces in the NFRP model. (a) V_c = 12 m/min. (b) V_c = 32 m/min. (c) V_c = 80 m/min

Fig. 7(b), there is a factor of about 3 between FEM thrust force magnitudes and experimental cutting force magnitudes. This correlation issue is well known also in the 2D machining models of synthetic fiber composites [28, 31] and it can be due to the fiber spring-back as reported in [31]. The magnitude factor between FEM and experimental thrust forced in around 8.5 in [28] and around 9.33 in [31] for the same fiber orientation (90°). The magnitude factor of 3 found in the current model for machining NFRP is less than those of the synthetic composite model and this can be due to the fact that natural fibers have less spring-back intensity because of their high transverse elasticity.

It is important to note that the thermal effect during machining was not considered in this study. Indeed, the orthogonal cutting experiments were performed with a cutting length of 30 mm. The contact duration between the tool and the material is then between 0.15 s (for V_c = 12 m/min) and 0.022 s (for V_c = 80 m/min) which is low to generate a significant temperature rise with friction or high plastic deformation rate.

3.3 FEM prediction of the cutting behavior of natural fibers

The FEM model shows the difference in the cutting behavior of flax fibers when changing the cutting speed as clearly illustrated in Fig. 8. Flax fibers are highly deformed before cutting when machining with V_c = 12 m/min as shown in Fig. 8(a) where 29 µm of additional transverse deformation is occurred comparing with the cutting configuration of V_c = 80 m/min (Fig. 8(c)). This high deformation induces a high damage in both fibers and matrix before shearing. Fiber deformation before shearing decreases significantly by increasing the cutting speed (Fig. 8(a) ➔ (b) ➔ (c)) which decreases also the failure damages in the material. Increasing the failure damage decreases the material stiffness and, then, the cutting contact stiffness is reduced which favors the fiber deformation during the cutting operation.

To validate the FE model in terms of machined surface state, Fig. 9 compares the cutting behavior of flax fibers between the proposed FEM and SEM images of the machined surfaces obtained by experiments. Machining with low cutting speed (V_c = 12 m/min) favors the fiber deformation before shearing which increases the debonding zones (DZ in Fig. 9) because of the fracture of the interfaces in addition to the torn-off of fibers that have poor maintenance during cutting. These defect phenomena are clearly obvious in both FEM (Fig. 9(a)) and experimental results (see Fig. 9(d)) where flax fibers are highly deformed which induces important DZ defects. When increasing the cutting speed, both FEM and experimental results show the increase of the fibers shearing efficiency and a reduction of the DZ defects by reducing the fiber deformation before shearing. This demonstrates that increasing the cutting speed increases the cutting contact stiffness which improves the shearing efficiency of flax fibers.

Moreover, Fig. 9 shows that the FE model can reproduce the same order of magnitude for the maximum debonding zone separation when comparing with the SEM images of the experimental machined surfaces. Indeed, from the SEM images of Fig. 9, the maximum DZ separation is founded around 28 µm for V_c = 12 m/min, 9 µm for V_c = 32 m/min, and 3 µm for V_c = 80 m/min which is closer to the DZ separation values obtained by FEM in Fig. 9(a–c).

3.4 FEM analysis of the cohesive interfaces after machining

FEM analysis has the advantage to allow the evaluation of the quality of interfaces, which is very complicated with physical experiments. Figure 10 presents the quadratic damage criterion map for the cohesive interfaces after the cutting operation. Machining at low cutting speed (V_c = 12 m/min) induces the highest interface defects as shown in Fig. 10(a). Increasing the cutting speed from 12 to 80 m/min leads to the decrease of the interfaces damage by ~ 43% which is really important to consider because interface defects in composite materials can

usually be the origin of the crack initiation through the composite part in service. The interface defects are mostly induced by the transverse fiber deformation that implies an in-plane shear (mode II) of the cohesive elements. Therefore, cutting with low cutting speed increases the fiber deformation before shearing (as shown in Section 3.3) which favors the interface defects. Inversely, increasing the cutting speed reduces the fiber deformation before shearing which limits the interface defects.

4 Conclusions

In this paper, a finite element analysis (FEA) is performed for the machining of natural fiber-reinforced polymer (NFRP) composites. A 2D micromechanical model is developed and finite element analysis is carried out in order to simulate each composite phase separately (fibers, matrix, and interfaces). Unidirectional flax fiber-reinforced polypropylene (PP) composite is considered in this study. Both flax fibers and PP matrix are modeled using an elasto-plastic behavior. The anisotropy of flax fibers is modeled using Hill's potential function. A dynamic mechanical behavior of PP matrix is considered due to its high plasticity. A ductile criterion based on the tress triaxiality is chosen for modeling the failure of flax fibers and PP matrix. The interfaces are modeled using the cohesive zone model (CZM) with a traction-separation law and quadratic damage criterion. The finite element analysis is carried out at different cutting speed values (from 12 to 80 m/min). The FEA results are validated with orthogonal cutting experiments at the same cutting conditions. The following conclusions can be drawn:

- The proposed finite element approach can predict efficiently the cutting force in terms of trend and magnitude. The thrust force trend is well reproduced. However, the thrust force magnitude is lower than experimental values with a factor of ~ 3. This could be due to the fiber springback after shearing.
- The proposed FE model can predict accurately the cutting behavior of flax fibers within the composite in terms of fiber deformation, fibers torn-off, and the debonding zones induced by the interfaces fracture.
- The proposed FE model allows the qualification of the machining sub-surface damages occurred in NFRP composite using a cohesive zone modeling of the interfaces.
- As a perspective, the proposed FE model needs to be adapted and validated at macroscale in order to generate a numerical predictive tool for industrial applications.

Funding information This study was financially supported by the urban community of Châlons-en-Champagne (*Cités en Champagne - France*).

References

1. Shalwan A, Yousif BF (2013) In state of art: mechanical and tribological behaviour of polymeric composites based on natural fibres. Mater Des 48:14–24. https://doi.org/10.1016/j.matdes.2012.07.014
2. Dittenber DB, GangaRao HVS (2012) Critical review of recent publications on use of natural composites in infrastructure. Compos Part A Appl Sci Manuf 43:1419–1429
3. Pickering KL, Aruan Efendy MG, Le TM (2016) A review of recent developments in natural fibre composites and their mechanical performance. Compos Part A Appl Sci Manuf 83:98–112. https://doi.org/10.1016/J.COMPOSITESA.2015.08.038
4. Wambua P, Ivens J, Verpoest I (2003) Natural fibres: can they replace glass in fibre reinforced plastics? Compos Sci Technol 63:1259–1264. https://doi.org/10.1016/S0266-3538(03)00096-4
5. Etaati A, Mehdizadeh SA, Wang H, Pather S (2014) Vibration damping characteristics of short hemp fibre thermoplastic composites. J Reinf Plast Compos 33:330–341. https://doi.org/10.1177/0731684413512228
6. Rajeshkumar G, Hariharan V (2014) Free vibration characteristics of Phoenix Sp fiber reinforced polymer matrix composite beams. Procedia Eng 97:687–693. https://doi.org/10.1016/J.PROENG.2014.12.298
7. Alves C, Ferrao PMC, Silva AJ et al (2010) Ecodesign of automotive components making use of natural jute fiber composites. J Clean Prod 18:313–327. https://doi.org/10.1016/J.JCLEPRO.2009.10.022
8. Ramesh M, Palanikumar K, Hemachandra Reddy K (2017) Plant fibre based bio-composites: sustainable and renewable green materials. Renew Sust Energ Rev 79:558–584. https://doi.org/10.1016/J.RSER.2017.05.094
9. Nassar MMA, Arunachalam R, Alzebdeh KI (2017) Machinability of natural fiber reinforced composites: a review. Int J Adv Manuf Technol 88:2985–3004. https://doi.org/10.1007/s00170-016-9010-9
10. Chegdani F, Mezghani S, El Mansori M, Mkaddem A (2015) Fiber type effect on tribological behavior when cutting natural fiber reinforced plastics. Wear 332–333:772–779. https://doi.org/10.1016/j.wear.2014.12.039
11. Chegdani F, El Mansori M (2018) Friction scale effect in drilling natural fiber composites. Tribol Int 119:622–630. https://doi.org/10.1016/j.triboint.2017.12.006
12. Chegdani F, Mezghani S, El Mansori M (2016) On the multiscale tribological signatures of the tool helix angle in profile milling of woven flax fiber composites. Tribol Int 100:132–140. https://doi.org/10.1016/j.triboint.2015.12.014
13. Chegdani F, Mezghani S, El Mansori M (2015) Experimental study of coated tools effects in dry cutting of natural fiber reinforced plastics. Surf Coat Technol 284:264–272. https://doi.org/10.1016/j.surfcoat.2015.06.083
14. Chegdani F, El Mansori M (2018) New multiscale approach for machining analysis of natural fiber reinforced bio-composites. J Manuf Sci Eng 141:11004. https://doi.org/10.1115/1.4041326
15. Baley C (2002) Analysis of the flax fibres tensile behaviour and analysis of the tensile stiffness increase. Compos Part A Appl Sci Manuf 33:939–948. https://doi.org/10.1016/S1359-835X(02)00040-4
16. Mackerle J (1999) Finite-element analysis and simulation of machining: a bibliography (1976–1996). J Mater Process Technol 86:17–44. https://doi.org/10.1016/S0924-0136(98)00227-1
17. Mackerle J (2003) Finite element analysis and simulation of machining: an addendum: a bibliography (1996–2002). Int J Mach Tools Manuf 43:103–114. https://doi.org/10.1016/S0890-6955(02)00162-1

18. Komvopoulos K, Erpenbeck SA (1991) Finite element modeling of orthogonal metal cutting. J Eng Ind 113:253. https://doi.org/10.1115/1.2899695
19. Johnson GR, Cook WH (1985) Fracture characteristics of three metals subjected to various strains, strain rates, temperatures and pressures. Eng Fract Mech 21:31–48. https://doi.org/10.1016/0013-7944(85)90052-9
20. Dixit US, Joshi SN, Davim JP (2011) Incorporation of material behavior in modeling of metal forming and machining processes: a review. Mater Des 32:3655–3670. https://doi.org/10.1016/J.MATDES.2011.03.049
21. Arrazola PJ, Özel T, Umbrello D, Davies M, Jawahir IS (2013) Recent advances in modelling of metal machining processes. CIRP Ann 62:695–718. https://doi.org/10.1016/J.CIRP.2013.05.006
22. Dandekar CR, Shin YC (2012) Modeling of machining of composite materials: a review. Int J Mach Tools Manuf 57:102–121. https://doi.org/10.1016/j.ijmachtools.2012.01.006
23. Venu Gopala Rao G, Mahajan P, Bhatnagar N (2007) Machining of UD-GFRP composites chip formation mechanism. Compos Sci Technol 67:2271–2281. https://doi.org/10.1016/J.COMPSCITECH.2007.01.025
24. Rao GVG, Mahajan P, Bhatnagar N (2007) Micro-mechanical modeling of machining of FRP composites – cutting force analysis. Compos Sci Technol 67:579–593. https://doi.org/10.1016/j.compscitech.2006.08.010
25. Dandekar CR, Shin YC (2008) Multiphase finite element modeling of machining unidirectional composites: prediction of debonding and fiber damage. J Manuf Sci Eng 130:51016. https://doi.org/10.1115/1.2976146
26. Gao C, Xiao J, Xu J, Ke Y (2016) Factor analysis of machining parameters of fiber-reinforced polymer composites based on finite element simulation with experimental investigation. Int J Adv Manuf Technol 83:1113–1125. https://doi.org/10.1007/s00170-015-7592-2
27. Mahdi M, Zhang L (2001) A finite element model for the orthogonal cutting of fiber-reinforced composite materials. J Mater Process Technol 113:373–377. https://doi.org/10.1016/S0924-0136(01)00675-6
28. Arola D, Ramulu M (1997) Orthogonal cutting of fiber-reinforced composites: a finite element analysis. Int J Mech Sci 39:597–613. https://doi.org/10.1016/S0020-7403(96)00061-6
29. Nayak D, Bhatnagar N, Mahajan P (2005) Machining studies of UD-FRP composites part 2: finite element analysis. Mach Sci Technol 9:503–528. https://doi.org/10.1080/10910340500398183
30. Santiuste C, Soldani X, Miguélez MH (2010) Machining FEM model of long fiber composites for aeronautical components. Compos Struct 92:691–698. https://doi.org/10.1016/J.COMPSTRUCT.2009.09.021
31. Lasri L, Nouari M, El Mansori M (2009) Modelling of chip separation in machining unidirectional FRP composites by stiffness degradation concept. Compos Sci Technol 69:684–692. https://doi.org/10.1016/J.COMPSCITECH.2009.01.004
32. Ghafarizadeh S, Chatelain J-F, Lebrun G (2016) Finite element analysis of surface milling of carbon fiber-reinforced composites. Int J Adv Manuf Technol 87:399–409. https://doi.org/10.1007/s00170-016-8482-y
33. Charlet K, Baley C, Morvan C, Jernot JP, Gomina M, Bréard J (2007) Characteristics of Hermès flax fibres as a function of their location in the stem and properties of the derived unidirectional composites. Compos Part A Appl Sci Manuf 38:1912–1921. https://doi.org/10.1016/j.compositesa.2007.03.006
34. Placet V, Cissé O, Lamine Boubakar M (2014) Nonlinear tensile behaviour of elementary hemp fibres. Part I: investigation of the possible origins using repeated progressive loading with in situ microscopic observations. Compos Part A Appl Sci Manuf 56:319–327. https://doi.org/10.1016/J.COMPOSITESA.2012.11.019
35. Keryvin V, Lan M, Bourmaud A, Parenteau T, Charleux L, Baley C (2015) Analysis of flax fibres viscoelastic behaviour at micro and nano scales. Compos Part A Appl Sci Manuf 68:219–225. https://doi.org/10.1016/J.COMPOSITESA.2014.10.006
36. Chegdani F, El Mansori M, Mezghani S, Montagne A (2017) Scale effect on tribo-mechanical behavior of vegetal fibers in reinforced bio-composite materials. Compos Sci Technol 150:87–94. https://doi.org/10.1016/j.compscitech.2017.07.012
37. Chegdani F, Wang Z, El Mansori M, Bukkapatnam STS (2018) Multiscale tribo-mechanical analysis of natural fiber composites for manufacturing applications. Tribol Int 122:143–150. https://doi.org/10.1016/j.triboint.2018.02.030
38. Chegdani F, El Mansori M (2018) Mechanics of material removal when cutting natural fiber reinforced thermoplastic composites. Polym Test 67:275–283. https://doi.org/10.1016/j.polymertesting.2018.03.016
39. Richard F, Poilâne C, Yang H, Gehring F, Renner E (2018) A viscoelastoplastic stiffening model for plant fibre unidirectional reinforced composite behaviour under monotonic and cyclic tensile loading. Compos Sci Technol 167:396–403. https://doi.org/10.1016/J.COMPSCITECH.2018.08.020
40. Panamoottil SM, Das R, Jayaraman K (2017) Towards a multiscale model for flax composites from behaviour of fibre and fibre/polymer interface. J Compos Mater 51:859–873. https://doi.org/10.1177/0021998316654303
41. Xiong X, Shen SZ, Hua L, Liu JZ, Li X, Wan X, Miao M (2018) Finite element models of natural fibers and their composites: a review. J Reinf Plast Compos 37:617–635. https://doi.org/10.1177/0731684418755552
42. Lefeuvre A, Bourmaud A, Lebrun L, Morvan C, Baley C (2013) A study of the yearly reproducibility of flax fiber tensile properties. Ind Crop Prod 50:400–407. https://doi.org/10.1016/j.indcrop.2013.07.035
43. Hearle JWS (1963) The fine structure of fibers and crystalline polymers. III Interpretation of the mechanical properties of fibers. J Appl Polym Sci 7:1207–1223. https://doi.org/10.1002/app.1963.070070403
44. Shah DU, Schubel PJ, Licence P, Clifford MJ (2012) Determining the minimum, critical and maximum fibre content for twisted yarn reinforced plant fibre composites. Compos Sci Technol 72:1909–1917. https://doi.org/10.1016/J.COMPSCITECH.2012.08.005
45. (2011) Abaqus Analysis User's Manual. In: Abaqus 6.11 Documentation. Dassault Systèmes Simulia Corp., Providence
46. Hooputra H, Gese H, Dell H, Werner H (2004) A comprehensive failure model for crashworthiness simulation of aluminium extrusions. Int J Crashworthiness 9:449–464. https://doi.org/10.1533/ijcr.2004.0289
47. Danas K, Ponte Castañeda P (2012) Influence of the Lode parameter and the stress triaxiality on the failure of elasto-plastic porous materials. Int J Solids Struct 49:1325–1342. https://doi.org/10.1016/J.IJSOLSTR.2012.02.006
48. Lin S, Xia Y, Lin C, et al (2013) Stress state dependent failure loci of a talc-filled polypropylene material under static loading and dynamic loading. In: 13th International Conference on Fracture. Beijing, pp 1–16
49. Gao Y, Ko JH, Lee HP (2018) 3D coupled Eulerian-Lagrangian finite element analysis of end milling. Int J Adv Manuf Technol 98:849–857. https://doi.org/10.1007/s00170-018-2284-3